batteries

MDPI

Article

Integrated Arrays of Micro Resistance Temperature Detectors for Monitoring of the Short-Circuit Point in Lithium Metal Batteries

Lianqi Zhao [1], Cong Wu [1], Xinshui Zhang [1], Yue Zhang [1], Chao Zhang [1], Lei Dong [2,*], Longxing Su [1,3,*] and Jin Xie [1]

[1] School of Physical Science and Technology, ShanghaiTech University, Shanghai 201210, China
[2] State Key Laboratory of Solidification Processing, Center of Advanced Lubrication and Seal Materials, School of Materials Science and Engineering, Northwestern Polytechnical University, Xi'an 710072, China
[3] School of Microelectronics, Southern University of Science and Technology, Shenzhen 518055, China
* Correspondence: donglei@nwpu.edu.cn (L.D.); sulx@sustech.edu.cn (L.S.)

Abstract: Short-circuit induced thermal runaway is one of the main obstacles that hinder the large-scale commercial applications of lithium metal batteries. The fast and accurate detection of an internal short-circuit is, therefore, a key step for preventing thermal runaway. The traditional temperature detection is mainly to place temperature sensors outside the battery, which is far from the actual hotspot inside the cell and has a lag in response. In this study, we integrated arrays of micro resistance temperature detectors (AMRTDs) inside the pouch cell. AMRTDs can be used for the detection of a short-circuit with a high temporal and spatial resolution. We show that the initial short-circuit may induce a high temperature local hotspot exceeding 300 °C, whereas the nearby area was still maintained at near room temperature. Our work provides a design strategy for in-situ detection of short-circuits in lithium metal batteries.

Keywords: in situ temperature measurement; resistance temperature detector; short-circuit detection; lithium metal batteries; thermal runaway; integrated arrays

Citation: Zhao, L.; Wu, C.; Zhang, X.; Zhang, Y.; Zhang, C.; Dong, L.; Su, L.; Xie, J. Integrated Arrays of Micro Resistance Temperature Detectors for Monitoring of the Short-Circuit Point in Lithium Metal Batteries. *Batteries* **2022**, *8*, 264. https://doi.org/10.3390/batteries8120264

Academic Editor: Carlos Ziebert

Received: 28 October 2022
Accepted: 29 November 2022
Published: 30 November 2022

1. Introduction

The growing global energy demand has promoted the installation of renewable energy systems, and the intermittent characteristics of renewable energy have further put forward high requirements for energy storage devices with high energy densities [1]. Therefore, the high-capacity lithium metal anode (3860 mAh g^{-1}) is replacing the traditional graphite anode (372 mAh g^{-1}) as the next-generation lithium battery [2–4]. However, during the charging process, lithium tends to deposit in the dendritic form, which may penetrate the separator. The formation of lithium dendrites may lead to a short-circuit of the cell, which even causes thermal runaway and catastrophic fires [5]. Safety is one of the greatest challenges that must be surmounted before the lithium metal anode can be widely applied for commercial applications [6]. There has been intense research on battery materials to improve the overall safety of lithium batteries [7–14], but it remains a grand challenge to completely prevent the battery from short-circuiting under different circumstances. Therefore, it is of great importance to monitor the internal temperature of lithium metal batteries to avoid a disaster caused by a short-circuit that may threaten personal safety and property safety [15–20].

Thermal runaway caused by a short-circuit inside the lithium battery is the most common failure mechanism for lithium ion batteries [21,22]. This usually goes through the following processes: (1) The hotspot induces the decomposition of the solid electrolyte interphase (SEI) and the reaction of active lithium with the organic solvent, which will further raise the temperature. (2) When the temperature rises to the melting point of the

separator (PP/PE ~130 °C), it will lead to an obvious short-circuit and the temperature will rise significantly. (3) A further increase in temperature leads to the decomposition of the positive electrode, releasing oxygen and heat. Meanwhile, the reaction will become irreversible until the reactants are completely consumed [23,24]. The short-circuit can be triggered either by internal lithium dendrite formation or external nail penetration [25,26]. Depending on the nature of different types of short-circuits, they might lead to a temperature rise locally, to different extents, and therefore eventually cause thermal failure at a different time [18–21,27]. For instance, the short-circuit due to the micro-sized lithium dendrite in lithium batteries typically has little effect on the temperature of most areas at the initial stage, but it can quickly develop into a thermal runaway. Therefore, the early detection of a short-circuit is important, and such detection requires both a high temporal resolution and a spatial resolution [15]. Typical solutions to measure the temperature of lithium batteries include non-contact methods and contact methods. Non-contact detection methods, such as infrared imaging [21,28], can obtain the macroscopic temperature distribution of the lithium battery remotely. However, the spatial resolution is often limited [29]. Contact detection methods, which rely on temperature sensors such as thermocouples, and resistance temperature detectors (RTDs) are generally combined with the simulation model to obtain temperature distribution [30–32]. More specifically, the contact detection methods for lithium batteries can be divided into two general categories including non-invasive temperature detection (outside the cell) and invasive temperature detection (inside the cell) [33,34]. The non-invasive temperature detection has the advantages of easy detection, and it does not affect the operation of the lithium battery. However, it can only reflect the surface temperature of the battery [35–37]. Therefore, invasive temperature detection has been used inside the cell in some recent works [21,38]. For example, the current density distribution inside the lithium battery is uneven due to the existence of the tabs. Such differences in current density distribution can cause differences in temperature in lithium batteries because of joule heat and heat dissipation differences. These temperature differences can be measured by these macroscopic detection methods. Nevertheless, most invasive detection methods still failed to detect the early short-circuit due to their poor spatial resolution [39,40]. The small length scales of lithium dendrites require temperature sensing at a more microscopic level [41]. For invasive temperature detection, temperature sensors can fall into three main categories: thermocouples, thermally sensitive resistors (thermistors), and RTDs [42]. The thermocouple consists of two dissimilar electrical conductors forming an electrical junction, in which temperature-dependent voltage is measured as a result of the Seebeck effect. Traditional thermocouples are not capable of determining temperature at a microscopic position because of their large size. The thermistor has a typical operating temperature range of −55 °C to +150 °C and is not suitable for measuring the short-circuit temperature of lithium batteries. Among different temperature sensors, the resistance temperature detector (RTD) is a pure metal resistor, typically platinum (Pt), nickel (Ni), or aurum (Au). The material has an accurate resistance/temperature relationship which can be used to indicate temperature. Typically, in the −50 to 600 °C temperature range, the linear change of resistance with temperature is as follows:

$$R_t = R_i + \alpha_t \Delta T$$

where R_t and R_i are the resistance of an RTD at t °C and t_i °C, respectively; α_t is the temperature coefficient of an RTD; and ΔT is the temperature difference between t and t_i. The resistance of metal crystals comes from crystal defects and phonons generated by thermal shock, and crystal defects are generally independent of temperature. In the range of −50–600 °C, the phonon density of metal crystals is proportional to temperature, so its resistance and temperature can be described by this linear function. Hence, depending on the exact type of metal resistor being used, RTDs are more suitable for measuring the internal temperature of lithium batteries due to their higher accuracy and repeatability, typically under 600 °C. However, due to the complexity in the lithium battery, the produc-

tion of RTD needs to use corrosion-resistant precious metals. Thus, the cost of AMRTDs' fabrication is one of the main limitations for the practical applications.

In this work, the micro-RTDs were fabricated by photolithography processes to accurately measure the temperature of the short-circuit point (Supplementary Figure S1). Multiple micro-RTDs in different locations form the arrays of micro-RTDs (AMRTDs). As a proof of concept, we have shown that AMRTDs can detect the temperature at the short-circuit point and the surrounding location at the same time inside a lithium battery to evaluate the effect of the short-circuit on the battery temperature. Ultra-thin polyimide (PI, 5 μm) was used to separate AMRTDs and the current collector inside the battery, which made AMRTD as close as possible to the battery's short-circuit point to obtain realistic temperature responses. The thick PI will not only reduce the detection accuracy but also affect heat dissipation (Supplementary Figure S2). The formation of lithium dendrite did not cause the temperature to rise until there was enough lithium metal to form a continuous short-circuit between the positive and negative electrodes. Subsequently, the temperature of the local hotspot exceeded 300 °C, whereas the nearby area was still maintained at nearly room temperature. The temperature of the short-circuit point and the surrounding area inside the lithium metal battery was successfully captured with a high temporal and spatial resolution through the AMRTDs.

2. Results

The AMRTDs were integrated inside the cell through micro/nano fabrication technology to detect the temperature response of localized hotspots. An ultrathin PI film (5 μm) was used to separate the AMRTDs from current collectors inside the lithium metal battery considering the excellent chemical stability and electrical insulating properties of PI. Figure 1a is the schematic diagram of a battery integrated with AMRTDs, which consists of a Cu foil as the current collector for the lithium anode, a porous polyolefin separator, and $LiNi_{0.8}Co_{0.1}Mn_{0.1}O_2$ (NCM811) on an aluminum current collector as the cathode. By distributing the AMRTDs on the backside of the anode, we can obtain the temperature response of the locations where RTDs are located. The temperature measured by RTD is as close as possible to the position where lithium deposition occurs due to the ultra-thin thickness of PI, which is by far one of the closest operando temperature detection methods reported in the literature. The lithographic pattern of an individual RTD is shown in Figure 1b; the diameter of an individual micro-RTD is around 45 μm. Briefly, the PI film was obtained by spin coating a thin film of polyamic acid (PAA). It was then polymerized to form a layer of PI with a thickness of 5 μm by sequentially heating at 80, 110, 150, 200, and 250 °C. The corresponding AMRTDs pattern was fabricated on the PI with lithography (details of the fabrication can be found in the Methods section). The as-fabricated RTD was annealed prior to temperature measurement. To calibrate the temperature responses, the micro-RTD was placed in an environmental chamber to measure the resistance at different temperatures. The results are displayed in Figure 1c. The typical starting temperature of the thermal runaway of Li-ion batteries is between 200 and 300 °C [17,40]. In a wide temperature region from 30 to 330 °C, the resistance of micro-RTD increases linearly with temperature, which demonstrated its potential capability in capturing the temperature response prior to the thermal runaway. In addition, polyimide films have excellent heat resistance and can operate below 400 °C without degradation for long periods. Generally, a short-circuit caused by lithium dendrite is quite small; the 45 μm sized RTD will be able to detect the temperature response of the short-circuit point at an early stage if it is close enough. In comparison, the traditional thermal detector placed outside the battery will not be able to detect the temperature change until the temperature outside the battery starts to rise.

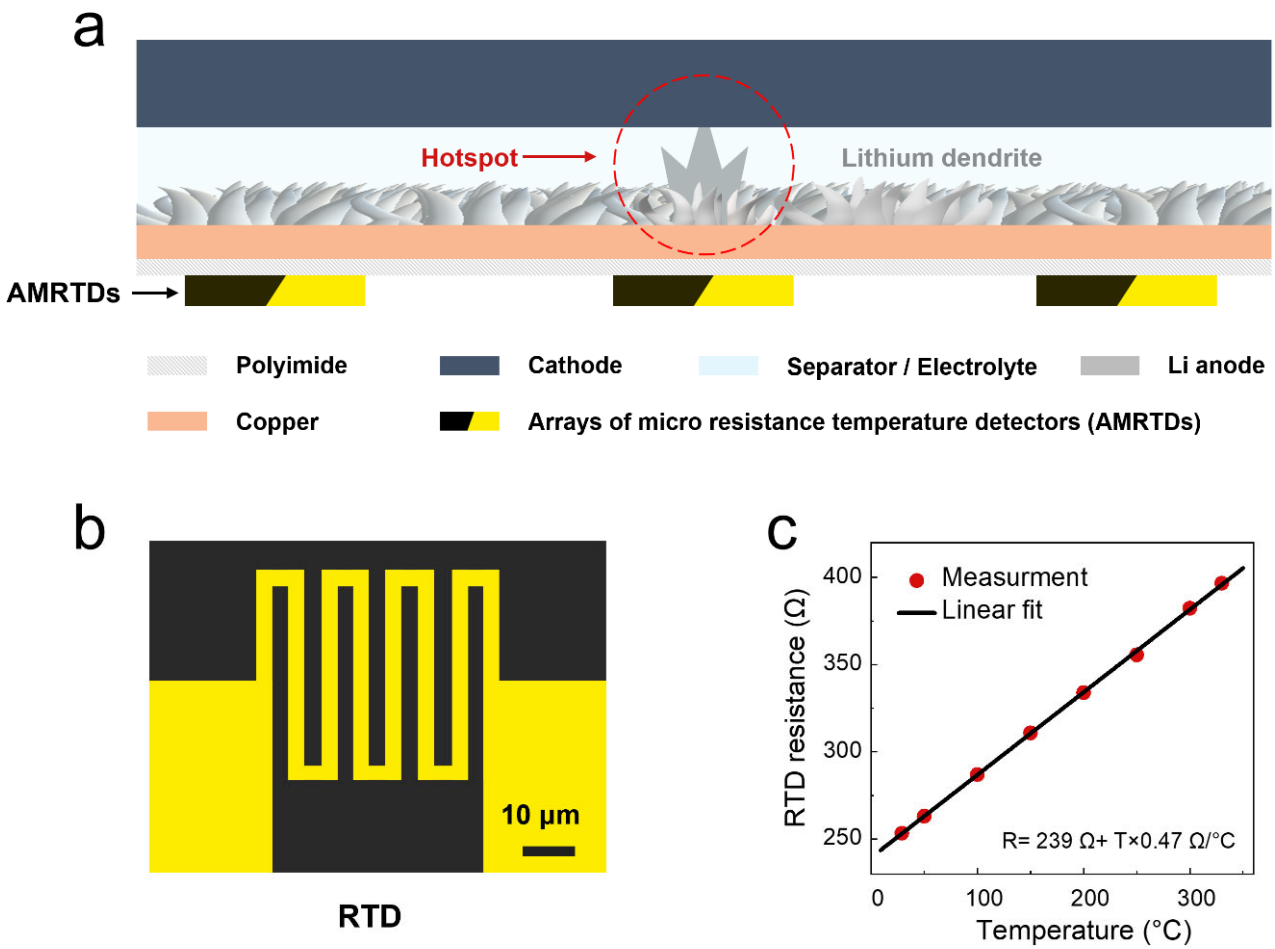

Figure 1. (**a**) Schematic illustration of the experimental setup of battery temperature measurement; (**b**) Lithographic design of RTD; (**c**) Calibration of the micro-RTD resistance as a function of the temperature.

As illustrated in Figure 2a, AMRTDs consist of a total of 10 micro-RTDs within the dotted line to obtain the global temperature distribution of lithium metal batteries simultaneously. The ten micro-RTDs are grouped to form five pairs to detect temperature responses at a different length scale. In more detail, micro-RTDs are separated by 400 μm, roughly an order of magnitude the size of the micro-RTD itself, within each pair. Figure 2b is the enlarged image of the area framed in Figure 2a, that contains a pair of micro-RTDs. Each pair of micro-RTDs is then further separated to 14 mm apart. The difference in distance allows us to better understand the temperature distribution across different length scales [28,38]. Figure 2c is an optical microscope image of Pt RTD obtained by micro/nano fabrication technology, consistent with Figure 2b. To better evaluate the lithium dendrite-induced shorting on temperature distributions, we then designed a circular hole in the separator to create a localized-temperature hotspot in the battery (Figure 2d, Supplementary Figure S3). To measure the short-circuit point temperature, we aligned the circular hole with one of the micro-RTDs (Figure 2d, Supplementary Figure S4). Through the AMRTDs, not only can the overall temperature distribution of the battery be obtained, but also the central temperature of the short-circuit point of the battery. In this study, we designed AMRTDs with a total of five pairs of micro-RTDs as a proof-of-concept to detect the local and global temperature response of the battery. In principle, more micro-RTDs with different combinations can be applied using similar fabrication approaches.

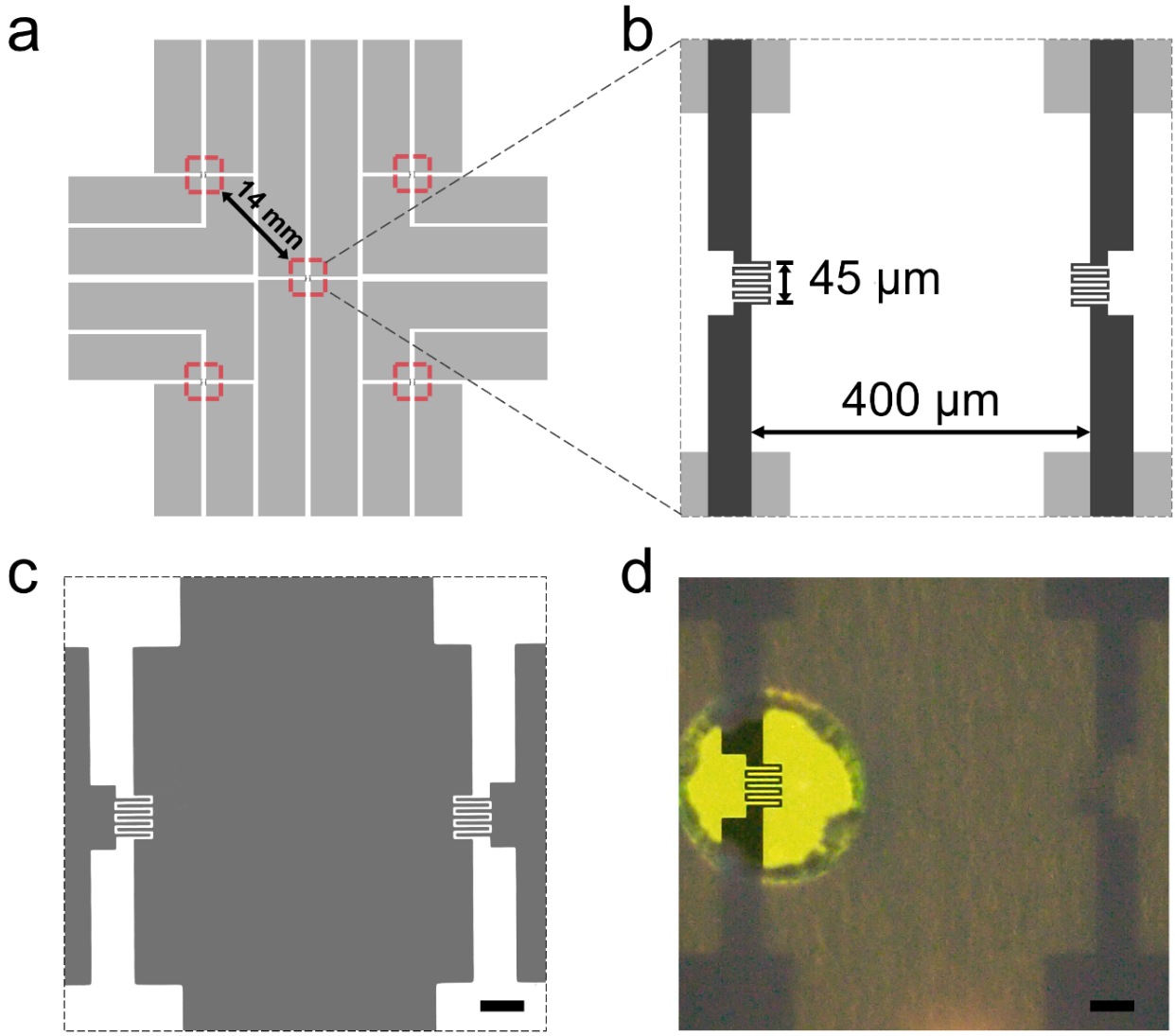

Figure 2. Fabrication of AMRTDs. (**a**) AMRTDs lithography design; (**b**) Enlarged image of a pair of micro-RTDs; (**c**) Optical image of a pair of micro-RTDs. scale bare, 50 μm; (**d**) Microscope image of aligned separator on one pair of micro-RTDs. scale bare, 50 μm.

The defects in the separator may affect the lithium deposition's morphology, which is a common battery failure mechanism, especially in lithium metal batteries. Figure 3 shows typical scanning electron microscopy (SEM) images of Li metal growths deposited onto Cu foil under 7 μm PE separators (SK) 1M $LiPF_6$ in 1:1 (*v*:*v*) ethylene carbonate (EC) and diethyl carbonate (DEC) at various current densities, ranging from 1 mA cm^{-2} and 2 mA cm^{-2} to 5 mA cm^{-2}. A vacuum transfer chamber was used to prevent the reaction of deposited Li from the ambient air. As shown in Figure 3a–c, the growth of lithium dendrites is quite uniform at different current densities. The insets in Figure 3a–c are enlarged images at each different current density, which clearly show the trends of thinner lithium dendrites at higher deposition rates. At a current density of 1mA cm^{-2} (Figure 3a), Li dendrites are thick on the Cu electrode's surface. As the current density increased (Figure 3b,c), the diameter of the Li dendrite decreased, and the Li dendrite become more closely packed. Nevertheless, the artificially introduced holes in the separator will significantly alter the lithium deposition's morphology underneath. For comparison, we designed a similar hole, shown in Figure 2d, and deposited lithium at a current density of 5 mA cm^{-2}. As shown in Figure 3d, the morphology and uniformity of Li dendrite in the region outside the hole (Figure 3d,e) is quite like those shown in Figure 3c. However, in the area inside

the hole (Figure 3f), the deposition of the Li dendrite is significantly enhanced (Figure 3e). There are two possible reasons for such enhanced lithium deposition. First, the porosity and tortuosity of the separator reduces the lithium-ion transportation, and therefore the ion flux significantly increases in the area without the separator and causes more lithium deposition [43]. Second, the existence of the separator also mechanically suppressed the formation of lithium dendrites, which leads to a relatively uniform deposition. To summarize, the separator may, to a certain degree, suppress the formation of lithium dendrites and lead to a more uniform lithium dendrite distribution. In contrast, in the case of defects in the separator, lithium dendrite may quickly form uneven depositions, which may then lead to battery shorting without the protection from the separator. The enhanced lithium deposition inside the hole will then lead to battery short-circuit. To further test the hypothesis, we made a hole with a similar size on a 7 µm thick separator and a 25 µm thick separator, respectively. As shown in Supplementary Figure S5, the time requirement for battery shorting is highly dependent on the thickness of the separator. In general, the coin cell with a 7 µm separator shorted at a much earlier time than that of the coin cell with a 25 µm separator. We then tested the shorting time in the pouch cell with different charging current densities of 1, 3, and 5 mA cm^{-2} using a 7 µm separator. The short-circuit time of the battery becomes shorter as the current density increases in the pouch cell (Supplementary Figure S6). The results further suggested that defects in separators could be a potential hazard for lithium metal batteries.

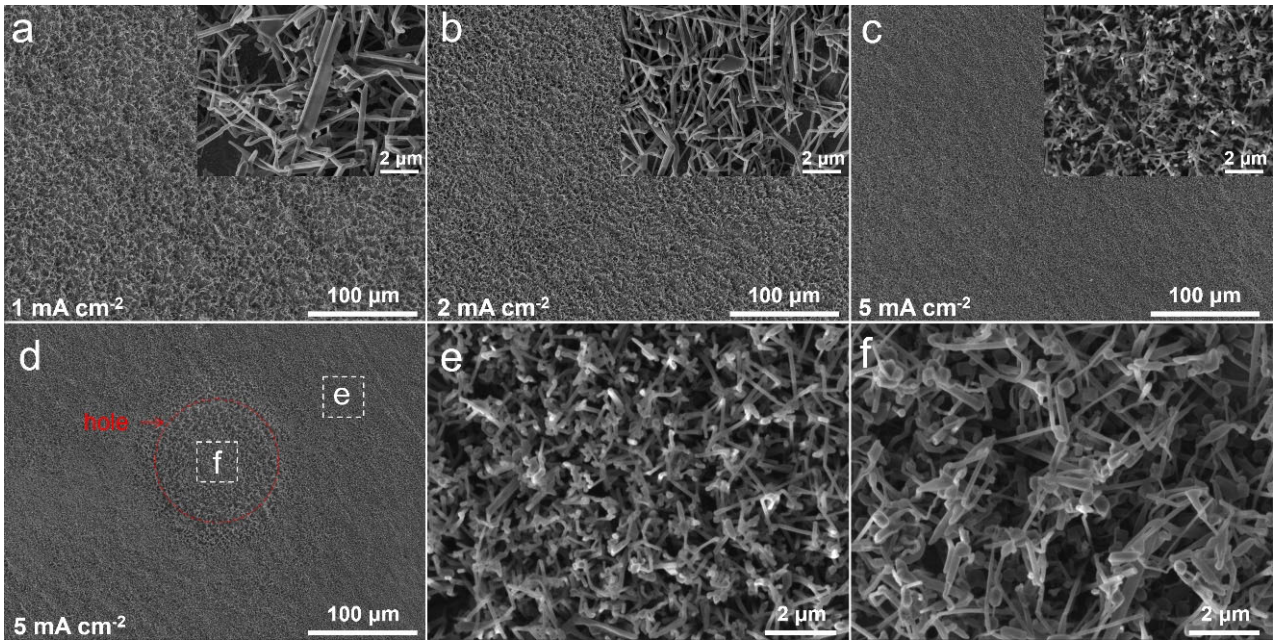

Figure 3. Lithium deposition morphology at different current densities. (**a**–**c**) SEM images of Li deposited on Cu at current densities of 1, 2, and 5 mA cm^{-2}, respectively, for a total areal capacity of 0.1 mAh cm^{-2} with a pristine separator; (**d**) SEM images of Li deposited on Cu at current densities of 5 mA cm^{-2} for a total areal capacity of 0.1 mAh cm^{-2} with a hole in the separator; (**e**,**f**) high magnification SEM images at different locations shown in Figure 3d.

We then investigated the in situ temperature response during battery shorting in a pouch cell using AMRTDs. A total of six micro-RTDs are monitored, and their relative positions are shown in Figure 4a. To obtain more accurate temperature distribution, an increased number of RTDs may be needed. The red circle in Figure 4a highlights the separator defects with a radius of 100 µm right above the micro-RTDs No.3. Figure 4b shows the cell voltage and cell temperature responses of a pouch cell charging at a current density of 5 mA cm^{-2}. The black line in Figure 4b is the battery voltage of the pouch cell. During the battery charging, the temperature responses of micro-RTDs at six different

positions were recorded in AMRTDs (labelled as No. 1–6). The battery started charging at t = 5 min. The initial voltage spike correlates with the nucleation barriers for lithium metal. In contrast with the smooth voltage curve initially, the battery voltage starts to fluctuate after t = 21 min, which represents a common feature for a micro-short-circuit beginning to occur in lithium metal batteries. The initial micro-short-circuit did not cause the temperature to rise immediately. During the whole charging process, the temperature was monitored by six micro-RTDs. Among them, No.1, No.2, No.5, and No.6 micro-RTDs did not detect significant temperature change. In contrast, both No.3 and No. 4 micro-RTDs had a remarkable temperature change. The temperature of No.3 micro-RTD started to rise and reached a maximum temperature of 300 °C at t = 56 min. At 400 µm away, No.4 micro-RTD reached a maximum temperature of 75 °C at t = 56 min. To our surprise, the temperature difference between this pair of micro-RTDs was more than 200 °C with a separation distance of only 400 µm. The pouch cell was then disassembled for optical microscope characterization. Indeed, accumulations of large lithium deposition were observed in the defect point of the separator next to the No. 3 micro-RTD (Supplementary Figure S7). In this experiment, we showed that a small defect in the separator can cause a battery to short-circuit within the first charging cycle and lead to a temperature hotspot of up to 300 °C. Nevertheless, the heat generated by the local hotspot is localized in the pouch cell that we tested. The maximum temperature dropped to 75 °C at a distance of 400 µm and further dropped to room temperature at a distance of 14 mm. Therefore, it represents a huge challenge for the early detection of battery shorting under realistic battery operation conditions for safety concerns.

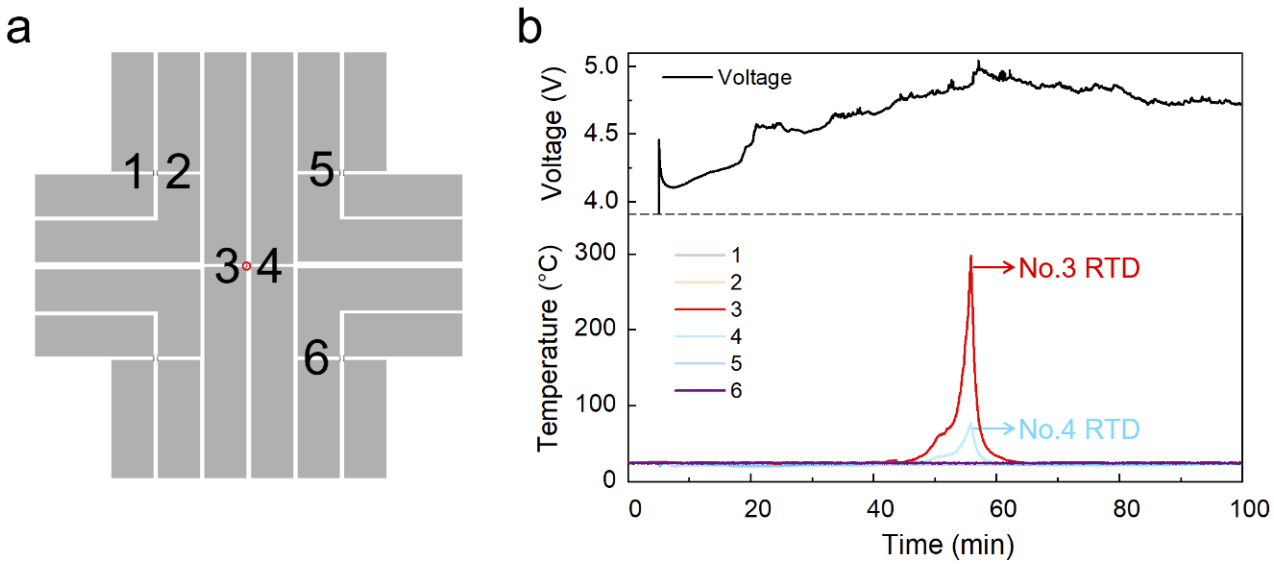

Figure 4. Temperature measurement by AMRTDs. (**a**) Relative positions of the 6 micro-RTDs on the AMRTD pattern. The red circle highlights the separator defects with a radius of 100 µm right above the No. 3 micro-RTD. (**b**) Cell voltage as the battery was charged at a constant current density of 5 mA cm^{-2}. The cell voltage of the battery (right axis) and temperature response at different locations measured by the micro-RTDs (left axis).

To further understand the temperature distribution in the pouch cell, a simplified model was used in COMSOL Multiphysics (Figure 5). The details of the model can be found in the Methods section. Figure 5a displayed a cross-sectional view of the layer-by-layer stack of the pouch cell model. A heat source was created by applying uniform volumetric heat generation in the battery's shorting region (7 µm thickness, 100 µm radius). The maximum power of the joule heat from the battery shorting is the product of the battery voltage and the charging current (225 mW). Figure 5b is the image of the temperature distribution of Figure 5a. It showed that the center temperature induced by the heat source (225 mW) can reach over 300 °C and gradually decreases towards the surroundings. It is

important to keep the micro-RTDs as close as possible to the current collector. Figure 5c shows the temperature distribution in the vertical direction from the micro-RTD surface (at the bottom of the PI film) to the Cu surface (at the top of the PI film), assuming different heating power. With the heat source at maximum power (225 mW), there is around a 30 °C temperature difference between the RTD (y = 0, T = 328 °C) and the center of the hotspot (y = 5 µm, T = 358 °C). The difference is 7 °C and 20 °C at a heating power of 50 mW and 150 mW. The result suggested that we should make the micro-RTD as close to the battery as possible for accurate battery temperature measurement. Figure 5d is the radial temperature distribution along the micro-RTD surface. For different heat source power, the temperature around the short-circuit point decreases rapidly. When the heat source is at maximum power (225 mW), the temperature measured by RTD No.3 is 328 °C at x = 0, and the temperature is 70 °C at x = 400 µm. The simulation agrees with the experiment, that a 400 µm separation is enough to cause a temperature difference up to more than 200 °C. As confirmed by both our measurement and simulation, the influence of the short-circuit temperature is concentrated in the local area and highlighted the difficulty in the early detection of battery shorting.

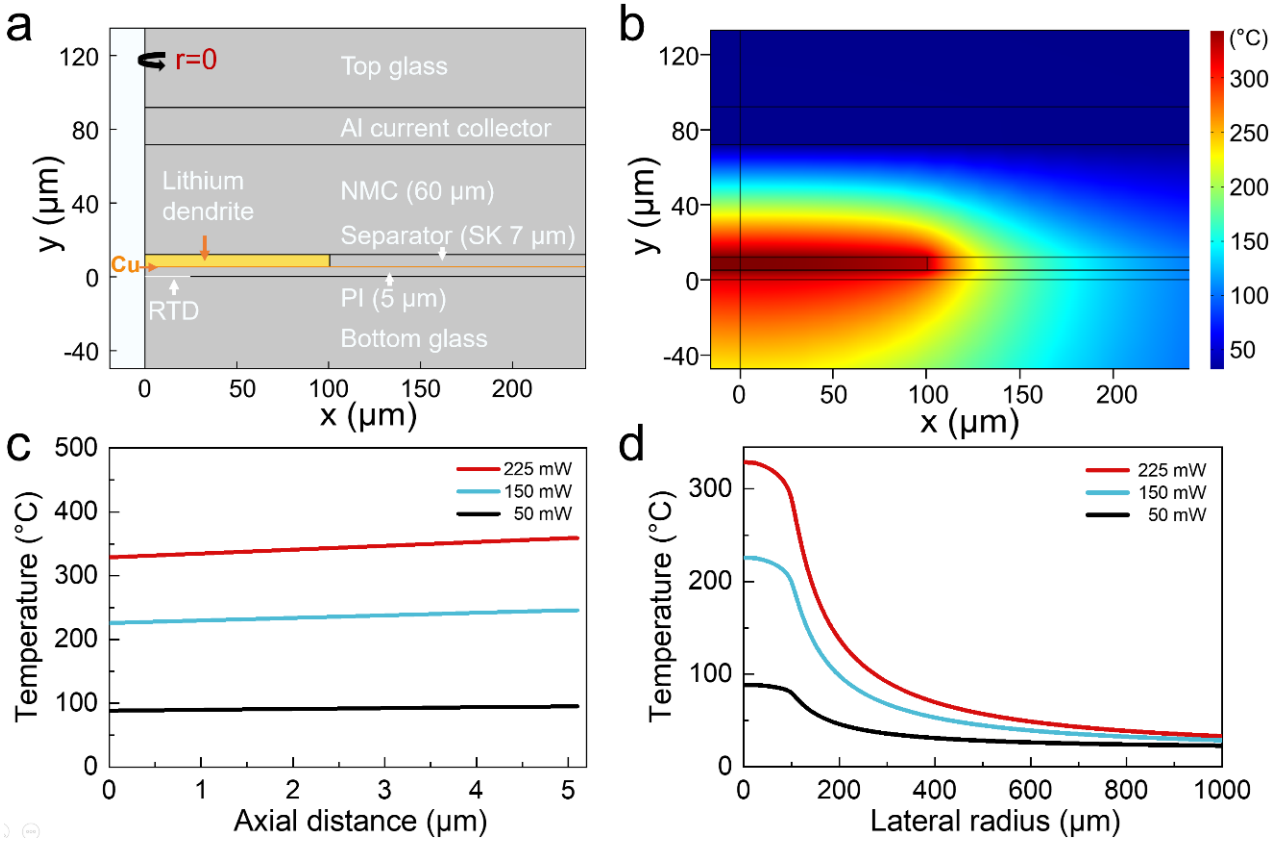

Figure 5. Thermal model. (**a**) Zoomed-in view of the thermal simulation cell. (**b**) Temperature distribution (zoomed-in side view); (**c**) Temperature distribution in the vertical direction from the RTD surface to the Cu surface; (**d**) The radial temperature profile along the RTD surface.

3. Materials and Methods

Arrays of micro-RTDs (AMRTDs) were fabricated on glass slide substrates (Sinopharm Chemical Reagent Co., Ltd. Shanghai, China, 92550108, 50 × 50 mm). The AMRTDs' pattern was obtained by a standard photolithography process. Subsequently, a 10 nm titanium (Ti) and a 50 nm platinum (Pt) were deposited onto the substrates. Then, the photoresist was removed by soaking it in PG Remover overnight. The Au AMRTDs were annealed at 300 °C for 2 h in an argon atmosphere. A 5 µm thick polyimide layer was spin-

coated and cured to cover the AMRTDs as an electrical insulation layer. All the micro-RTDs were calibrated at a stationary temperature.

The NCM811 electrodes were prepared by mixing NCM811 powders, Super P carbon black, and PVDF with a weight ratio of 8:1:1 in N-methyl pyrrolidine (NMP) using a THINKY MIXER. The slurry was cast onto Al foils and dried in a vacuum oven at 80 °C overnight. For the in situ temperature measurement, a 100 nm Cu layer was first sputtered on the PI as the working electrode. A separator (SK, 7 μm) was used to separate the working electrode and NCM811 cathode. A 100 μm radius aperture was made vertically above one of the micro-RTDs to induce a short-circuit. The electrolyte consisted of 1M $LiPF_6$ in 1:1 (*v*:*v*) EC/DEC. The typical loading of active materials is 16 mg cm^{-2}.

COMSOL model: The temperature profile as a result of the battery short-circuit was simulated using COMSOL Multiphysics with the "Heat Transfer in Solids" module. A two-dimensional (2D) geometry with rotation was built to form a three-dimensional (3D) model. The domain consists of a glass disk (1.5 mm thick, 8.5 mm in radius), an Al layer (20 μm thick, 8.5 mm in radius), an NCM layer (70 μm thick, 8.5 mm in radius), an electrolyte layer (7 μm thick, 8.5 mm in radius), a Cu layer (100 nm thick, 8.5 mm in radius), PI (5 μm thick, 8.5 mm in radius), and micro-RTD (50 nm thick, 22.5 μm in radius), which represents the experimental conditions. The porous separator, which is soaked in the electrolyte domain, was not considered in the simulation. This is because its thermal conductivity is similar to that of the electrolyte (both approximately 0.3 W/m×K). A heat source was created in the electrolyte by applying uniform volumetric heat generation in a region (7 μm in thickness, 100 μm in radius) to present the hole in the separator.

4. Conclusions

We fabricated AMRTDs through micro/nano fabrication and integrated them inside the pouch cell using an ultrathin PI film to ensure the AMRTDs were as close as possible to the short-circuit location. Furthermore, as a proof-of-concept, we used the AMRTDs for the in situ temperature measurement across different length scales. Our experimental results suggested that a short-circuit in lithium metal batteries can be induced by defects in the separator. The increase in temperature only occurred at a localized position, initially next to the battery's short-circuit location, as confirmed by both AMRTDs and the simulation results. The excellent resolution in both time and space of the AMRTDs inside the cell can detect high-temperature warnings in advance.

Supplementary Materials: The following supporting information can be downloaded at: https://www.mdpi.com/article/10.3390/batteries8120264/s1, Figure S1: Au and Pt micro-RTDs are fabricated by photolithography. Figure S2: Four simulated models with the different PI thickness of 5, 20, 50, and 100 μm. Figure S3: Optical pictures of separators with micropores for inducing lithium dendrite short circuits. Figure S4: Optical images of the aligned circular micropores in separator with the micro-RTD. Figure S5: Coin cell charging curve which used 7 μm or 25 μm thickness separator with a similar size micropore. Figure S6: Pouch cells charging curve which used a 7 μm thickness separator with a similar size micropore at a different charging current density of 1, 3, and 5 mA cm-2 respectively. Figure S7: Optical microscopy images of the negative electrode after charging.

Author Contributions: L.Z.: conceptualization, investigation, data curation, and writing—original draft. C.W.: investigation and data curation. L.D.: investigation and data curation. X.Z.: investigation and data curation. Y.Z.: investigation and data curation. C.Z.: investigation and data curation. L.S. and J.X.: conceptualization and writing—review and editing. All authors have read and agreed to the published version of the manuscript.

Funding: This work was supported by ShanghaiTech University (China) Startup Fund.

Data Availability Statement: Not applicable.

Acknowledgments: The authors thank the support from Soft Matter Nanofab (SMN180827), Shanghai Key Laboratory of High-resolution Electron Microscopy (Shanghai Science and Technology Plan, 21DZ2260400), the Center for High-Resolution Electron Microscopy (CħEM) (No. EM02161943), SPST, ShanghaiTech University, and the Analytical Instrumentation Center (#SPST-AIC10112914), SPST, ShanghaiTech University.

Conflicts of Interest: The authors declare no conflict of interest.

References

1. Larcher, D.; Tarascon, J.-M. Towards Greener and More Sustainable Batteries for Electrical Energy Storage. *Nat. Chem.* **2015**, *7*, 19–29. [CrossRef] [PubMed]
2. Xu, W.; Wang, J.; Ding, F.; Chen, X.; Nasybulin, E.; Zhang, Y.; Zhang, J.-G. Lithium Metal Anodes for Rechargeable Batteries. *Energy Environ. Sci.* **2014**, *7*, 513–537. [CrossRef]
3. Yan, X.; Lin, L.; Chen, Q.; Xie, Q.; Qu, B.; Wang, L.; Peng, D. Multifunctional Roles of Carbon-based Hosts for Li-metal Anodes: A Review. *Carbon Energy* **2021**, *3*, 303–329. [CrossRef]
4. Wang, C.; Adair, K.; Sun, X. All-Solid-State Lithium Metal Batteries with Sulfide Electrolytes: Understanding Interfacial Ion and Electron Transport. *Acc. Mater. Res.* **2022**, *3*, 21–32. [CrossRef]
5. Li, J.; Kong, Z.; Liu, X.; Zheng, B.; Fan, Q.H.; Garratt, E.; Schuelke, T.; Wang, K.; Xu, H.; Jin, H. Strategies to Anode Protection in Lithium Metal Battery: A Review. *InfoMat* **2021**, *3*, 1333–1363. [CrossRef]
6. Liu, B.; Zhang, J.-G.; Xu, W. Advancing Lithium Metal Batteries. *Joule* **2018**, *2*, 833–845. [CrossRef]
7. Chen, X.; Yan, S.; Tan, T.; Zhou, P.; Hou, J.; Feng, X.; Dong, H.; Wang, P.; Wang, D.; Wang, B.; et al. Supramolecular "Flame-Retardant" Electrolyte Enables Safe and Stable Cycling of Lithium-Ion Batteries. *Energy Storage Mater.* **2022**, *45*, 182–190. [CrossRef]
8. Ye, Y.; Chou, L.Y.; Liu, Y.; Wang, H.; Lee, H.K.; Huang, W.; Wan, J.; Liu, K.; Zhou, G.; Yang, Y.; et al. Ultralight and Fire-Extinguishing Current Collectors for High-Energy and High-Safety Lithium-Ion Batteries. *Nat. Energy* **2020**, *5*, 786–793. [CrossRef]
9. Yuan, M.; Liu, K. Rational Design on Separators and Liquid Electrolytes for Safer Lithium-Ion Batteries. *J. Energy Chem.* **2020**, *43*, 58–70. [CrossRef]
10. Cui, Y.; Wan, J.; Ye, Y.; Liu, K.; Chou, L.Y.; Cui, Y. A Fireproof, Lightweight, Polymer-Polymer Solid-State Electrolyte for Safe Lithium Batteries. *Nano Lett.* **2020**, *20*, 1686–1692. [CrossRef] [PubMed]
11. Zhou, G.; Liu, K.; Fan, Y.; Yuan, M.; Liu, B.; Liu, W.; Shi, F.; Liu, Y.; Chen, W.; Lopez, J.; et al. An Aqueous Inorganic Polymer Binder for High Performance Lithium-Sulfur Batteries with Flame-Retardant Properties. *ACS Cent. Sci.* **2018**, *4*, 260–267. [CrossRef] [PubMed]
12. Yuan, S.; Chang, C.; Yan, S.; Zhou, P.; Qian, X.; Yuan, M.; Liu, K. A Review of Fire-Extinguishing Agent on Suppressing Lithium-Ion Batteries Fire. *J. Energy Chem.* **2021**, *62*, 262–280. [CrossRef]
13. Iqbal, S.; Bahadur, A.; Saeed, A.; Zhou, K.; Shoaib, M.; Waqas, M. Journal of Colloid and Interface Science Electrochemical Performance of 2D Polyaniline Anchored CuS/Graphene Nano-Active Composite as Anode Material for Lithium-Ion Battery. *J. Colloid Interface Sci.* **2017**, *502*, 16–23. [CrossRef] [PubMed]
14. Bahadur, A.; Iqbal, S.; Shoaib, M.; Saeed, A. Electrochemical Study of Specially Designed Graphene-Fe_3O_4-Polyaniline Nanocomposite as a High-Performance Anode for Lithium-Ion Battery. *Dalton Trans.* **2018**, *47*, 15031–15037. [CrossRef] [PubMed]
15. Liu, B.; Jia, Y.; Yuan, C.; Wang, L.; Gao, X.; Yin, S.; Xu, J. Safety Issues and Mechanisms of Lithium-Ion Battery Cell upon Mechanical Abusive Loading: A Review. *Energy Storage Mater.* **2020**, *24*, 85–112. [CrossRef]
16. Xu, J.; Wang, H.; Shi, H.; Mei, X. Multi-Scale Short Circuit Resistance Estimation Method for Series Connected Battery Strings. *Energy* **2020**, *202*, 117647. [CrossRef]
17. Liu, X.; Ren, D.; Hsu, H.; Feng, X.; Xu, G.L.; Zhuang, M.; Gao, H.; Lu, L.; Han, X.; Chu, Z.; et al. Thermal Runaway of Lithium-Ion Batteries without Internal Short Circuit. *Joule* **2018**, *2*, 2047–2064. [CrossRef]
18. Wang, Q.; Mao, B.; Stoliarov, S.I.; Sun, J. A Review of Lithium Ion Battery Failure Mechanisms and Fire Prevention Strategies. *Prog. Energy Combust. Sci.* **2019**, *73*, 95–131. [CrossRef]
19. Abada, S.; Marlair, G.; Lecocq, A.; Petit, M.; Sauvant-Moynot, V.; Huet, F. Safety Focused Modeling of Lithium-Ion Batteries: A Review. *J. Power Sources* **2016**, *306*, 178–192. [CrossRef]
20. Feng, X.; Ouyang, M.; Liu, X.; Lu, L.; Xia, Y.; He, X. Thermal Runaway Mechanism of Lithium Ion Battery for Electric Vehicles: A Review. *Energy Storage Mater.* **2018**, *10*, 246–267. [CrossRef]
21. Chen, Z.; Xiong, R.; Tian, J.; Shang, X.; Lu, J. Model-Based Fault Diagnosis Approach on External Short Circuit of Lithium-Ion Battery Used in Electric Vehicles. *Appl. Energy* **2016**, *184*, 365–374. [CrossRef]
22. Chombo, P.V.; Laoonual, Y. A Review of Safety Strategies of a Li-Ion Battery. *J. Power Sources* **2020**, *478*, 228649. [CrossRef]
23. Finegan, D.P.; Scheel, M.; Robinson, J.B.; Tjaden, B.; Hunt, I.; Mason, T.J.; Millichamp, J.; Di Michiel, M.; Offer, G.J.; Hinds, G.; et al. In-Operando High-Speed Tomography of Lithium-Ion Batteries during Thermal Runaway. *Nat. Commun.* **2015**, *6*, 6924. [CrossRef] [PubMed]
24. Liu, K.; Liu, Y.; Lin, D.; Pei, A.; Cui, Y. Materials for Lithium-Ion Battery Safety. *Sci. Adv.* **2018**, *4*, eaas9820. [CrossRef]

25. Zhu, Y.; Xie, J.; Pei, A.; Liu, B.; Wu, Y.; Lin, D.; Li, J.; Wang, H.; Chen, H.; Xu, J.; et al. Fast Lithium Growth and Short Circuit Induced by Localized-Temperature Hotspots in Lithium Batteries. *Nat. Commun.* **2019**, *10*, 2067. [CrossRef]
26. Abaza, A.; Ferrari, S.; Wong, H.K.; Lyness, C.; Moore, A.; Weaving, J.; Blanco-Martin, M.; Dashwood, R.; Bhagat, R. Experimental Study of Internal and External Short Circuits of Commercial Automotive Pouch Lithium-Ion Cells. *J. Energy Storage* **2018**, *16*, 211–217. [CrossRef]
27. Maleki, H.; Howard, J.N. Internal Short Circuit in Li-Ion Cells. *J. Power Sources* **2009**, *191*, 568–574. [CrossRef]
28. Ramadass, P.; Fang, W.; Zhang, Z. Study of Internal Short in a Li-Ion Cell I. Test Method Development Using Infra-Red Imaging Technique. *J. Power Sources* **2014**, *248*, 769–776. [CrossRef]
29. Wang, S.; Li, K.; Tian, Y.; Wang, J.; Wu, Y.; Ji, S. Infrared Imaging Investigation of Temperature Fluctuation and Spatial Distribution for a Large Laminated Lithium–Ion Power Battery. *Appl. Therm. Eng.* **2019**, *152*, 204–214. [CrossRef]
30. Wang, Q.; Ping, P.; Zhao, X.; Chu, G.; Sun, J.; Chen, C. Thermal Runaway Caused Fire and Explosion of Lithium Ion Battery. *J. Power Sources* **2012**, *208*, 210–224. [CrossRef]
31. Saw, L.H.; Somasundaram, K.; Ye, Y.; Tay, A.A.O. Electro-Thermal Analysis of Lithium Iron Phosphate Battery for Electric Vehicles. *J. Power Sources* **2014**, *249*, 231–238. [CrossRef]
32. Ye, Y.; Shi, Y.; Cai, N.; Lee, J.; He, X. Electro-Thermal Modeling and Experimental Validation for Lithium Ion Battery. *J. Power Sources* **2012**, *199*, 227–238. [CrossRef]
33. Liu, H.; Wei, Z.; He, W.; Zhao, J. Thermal Issues about Li-Ion Batteries and Recent Progress in Battery Thermal Management Systems: A Review. *Energy Convers. Manag.* **2017**, *150*, 304–330. [CrossRef]
34. Ren, D.; Feng, X.; Liu, L.; Hsu, H.; Lu, L.; Wang, L.; He, X.; Ouyang, M. Investigating the Relationship between Internal Short Circuit and Thermal Runaway of Lithium-Ion Batteries under Thermal Abuse Condition. *Energy Storage Mater.* **2021**, *34*, 563–573. [CrossRef]
35. Song, W.; Chen, M.; Bai, F.; Lin, S.; Chen, Y.; Feng, Z. Non-Uniform Effect on the Thermal/Aging Performance of Lithium-Ion Pouch Battery. *Appl. Therm. Eng.* **2018**, *128*, 1165–1174. [CrossRef]
36. Walker, W.; Ardebili, H. Thermo-Electrochemical Analysis of Lithium Ion Batteries for Space Applications Using Thermal Desktop. *J. Power Sources* **2014**, *269*, 486–497. [CrossRef]
37. Forgez, C.; Vinh Do, D.; Friedrich, G.; Morcrette, M.; Delacourt, C. Thermal Modeling of a Cylindrical $LiFePO_4$/Graphite Lithium-Ion Battery. *J. Power Sources* **2010**, *195*, 2961–2968. [CrossRef]
38. Li, Z.; Zhang, J.; Wu, B.; Huang, J.; Nie, Z.; Sun, Y.; An, F.; Wu, N. Examining Temporal and Spatial Variations of Internal Temperature in Large-Format Laminated Battery with Embedded Thermocouples. *J. Power Sources* **2013**, *241*, 536–553. [CrossRef]
39. Lin, X.; Perez, H.E.; Siegel, J.B.; Stefanopoulou, A.G.; Li, Y.; Anderson, R.D.; Ding, Y.; Castanier, M.P. Online Parameterization of Lumped Thermal Dynamics in Cylindrical Lithium Ion Batteries for Core Temperature Estimation and Health Monitoring. *IEEE Trans. Control Syst. Technol.* **2013**, *21*, 1745–1755. [CrossRef]
40. Feng, X.; Fang, M.; He, X.; Ouyang, M.; Lu, L.; Wang, H.; Zhang, M. Thermal Runaway Features of Large Format Prismatic Lithium Ion Battery Using Extended Volume Accelerating Rate Calorimetry. *J. Power Sources* **2014**, *255*, 294–301. [CrossRef]
41. Chen, M.; Bai, F.; Lin, S.; Song, W.; Li, Y.; Feng, Z. Performance and Safety Protection of Internal Short Circuit in Lithium-Ion Battery Based on a Multilayer Electro-Thermal Coupling Model. *Appl. Therm. Eng.* **2019**, *146*, 775–784. [CrossRef]
42. Lee, C.Y.; Lee, S.J.; Tang, M.S.; Chen, P.C. In Situ Monitoring of Temperature inside Lithium-Ion Batteries by Flexible Micro Temperature Sensors. *Sensors* **2011**, *11*, 9942–9950. [CrossRef] [PubMed]
43. Cannon, A.; Ryan, E.M. Characterizing the Microstructure of Separators in Lithium Batteries and Their Effects on Dendritic Growth. *ACS Appl. Energy Mater.* **2021**, *4*, 7848–7861. [CrossRef]